Materials & Design 246 (2024) 113321

Contents lists available at ScienceDirect

Materials & Design

journal homepage: www.elsevier.com/locate/matdes

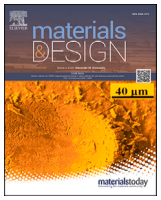

Predicting fatigue life of additively manufactured lattice structures using the image-based Finite Cell Method and average strain energy density

Raffaele De Biasi [a,1], Oguz Oztoprak [b,1], Filippo Zanini [c], Simone Carmignato [c], Stefan Kollmannsberger [b,*], Matteo Benedetti [a]

[a] Department of Industrial Engineering, University of Trento, Via Sommarive 9, Trento, 38123, Italy
[b] Chair of Data Science in Civil Engineering, Bauhaus-Universität Weimar, Coudraystr. 13b, Weimar, 99423, Germany
[c] Department of Management and Engineering, University of Padova, Stradella San Nicola 3, Vicenza, 36100, Italy

ARTICLE INFO

Dataset link: https://doi.org/10.14459/2024mp1751465

Keywords:
Lattice structure
Fatigue life estimation
Finite Cell Method
Strain energy density

ABSTRACT

A well-known Achilles' heel of laser powder bed fusion (L-PBF) additive manufactured lattice structures is the difficulty in predicting fatigue properties. The presence of manufacturing-induced defects significantly affects the fatigue resistance of the porous component and must be accurately captured by predictive models. To tackle this challenge, the as-built geometry of the lattice needs to be modeled, which introduces another challenge on the computational front. For the first time, a model based on the computer tomography (μ-CT) reconstruction of the as-built lattice geometry is simulated with the efficient finite cell method and combined with the average strain energy density (ASED) to obtain accurate fatigue predictions. This work presents a workflow for determining the fatigue resistance of lattice metamaterial, followed by a case study for method validation. The validation shows a good agreement between the predicted fatigue life and the experimental results.

1. Introduction

Lattice structures manufactured by the laser powder bed fusion (L-PBF) technology have gained widespread attention for their potential to deliver high-performing mechanical properties and lightweight characteristics. While the L-PBF process enables the manufacturing of complex and small-scale lattice structures, the resulting mechanical properties of the components can often be suboptimal due to geometrical imperfections introduced during the manufacturing process. Thus, realizing the potential of additively manufactured (AM) lattice structures requires considering the effects of manufacturing imperfections on the mechanical properties. To this end, numerical simulations offer a non-destructive approach to estimate critical mechanical properties. Yet, standard simulation workflows based on the as-designed CAD geometry fail to capture the significant impact of geometrical imperfections on the mechanical properties [1]. Therefore, numerical approaches have to consider the three-dimensional (3D) geometry of the as-built object, e.g. as captured through micro X-ray computed tomography (μ-CT).

Fatigue strength of metallic lattice structures is a key mechanical property that is adversely affected by process-induced internal pores and surface defects [2]. In some cases, the fatigue life can deteriorate more than an order of magnitude due to the presence of manufacturing defects [3,4]. The significant reduction of fatigue life due to process-induced pores and surface imperfections is widely considered one of the main factors impeding the industrial adoption of AM metallic lattice structures [2,5], e.g. for use in safety critical parts. Therefore, the research into the fatigue behavior of AM lattice structures continues to be widely active [6]. The equivalent von Mises stress [7] is used in conjunction with the theory of the critical distances (TCD) [8] to estimate the fatigue strength of AM lattice structures in [9,10]. Moreover, the Crossland criteria [11,12] is used as another stress-based approach to estimate fatigue life [13,14], however, the Crossland criteria can lead to imprecise predictions for AM parts, as the criteria is strongly influenced by how well stress singularities are resolved e.g. around notches. A criteria less sensitive to these effects is the average strain energy density (ASED). In [15] a comprehensive framework is established to account for notch sensitivity in fatigue life predictions [16], and it is applied to-

* Corresponding author.
E-mail address: stefan.kollmannsberger@uni-weimar.de (S. Kollmannsberger).
[1] The two authors have equally contributed and share the first authorship.

https://doi.org/10.1016/j.matdes.2024.113321
Received 23 July 2024; Received in revised form 30 August 2024; Accepted 14 September 2024
Available online 18 September 2024

gether with generalized extreme value (GEV) theory [17] to AM lattice structures in [18].

There is a growing amount of research focused on numerical approaches to study mechanical properties of AM lattice structures with emphasis on the as-built geometry [19]. Homogenized and statistics-based 3D numerical models were used to predict elastic and failure behavior of lattice samples by [20], where the key geometrical defects were reconstructed from μ-CT images. Similarly, [21] used the statistical finite element modeling of geometrical defects to investigate the impact of an individual geometric defect type (e.g. struct thickness variation, struct waviness) on the mechanical performance. [22] proposed an elliptical cross-section profile to reflect the as-built surface of AM lattices in computer-aided design (CAD) models, and this approach was used in conjunction with Monte Carlo (MCS) simulations to estimate the uncertainty associated with the mechanical response of lattice samples in [23]. Moreover, a multi-scale approach was proposed by [24], where the local mechanical properties of the lattices were estimated based on nano-indentation experiments and the as-built geometry of the whole specimen as acquired by μ-CT is used for numerical analysis. The contribution in [25] studied the effects of surface defects on the elastic modulus based on imperfect beam elements and solid finite element modeling of unit-cells. They concluded that the numerical analysis on the as-designed geometry showed a poor agreement with the experimental results. [26] analyzed the as-manufactured node elements within a lattice structure based on voxel-based finite elements. An image-based finite element approach using porous plasticity models was used in [27] to simulate the compression behavior of lattice specimens. Furthermore, [1] considers the entirety of an as-built lattice specimen to analyze the elastic modulus and bending rigidity, respectively, based on the image-based Finite Cell Method (FCM) [28,29]. The image-based FCM was recently extended to incorporate the Lemaitre damage model [30], enabling the investigation of local damage distribution in imperfect lattice cells [31]. The results further demonstrate the necessity to incorporate as-manufactured geometry into numerical analysis tools for accurate estimation of mechanical properties.

This contribution presents a workflow to predict the fatigue life of AM lattice components, directly utilizing the complete as-manufactured geometry captured by μ-CT for a numerical, non-destructive approach with image-based FCM, ASED approach, and extreme value statistics. The image-based FCM is used to directly simulate on the μ-CT-image, without a preprocessing step for 3D surface reconstruction, based on quasi-static loading conditions that replicate the experimental conditions. The ASED is then computed over the critical volume, where locations with high Von Mises stress are considered in the analysis. The resulting ASED values of the critical regions are assessed with extreme value statistics to predict fatigue failure based on the SED-N curve of the unnotched bulk specimen from [32].

The paper is organized as follows: in section 2, a theoretical and technical background of the techniques used is presented, followed in section 3.1 by a description of the methodology proposed. The second part of section 3.1 and section 4 are devoted to validating the method, describing its application, and discussing the results on a specific lattice geometry.

2. Background

The work presented in the manuscript is based on three technological and theoretical pillars: a micro X-ray computed tomography, the Finite Cell Method, and an average strain energy density criterion. These three are briefly recalled in this section.

2.1. Micro X-ray computed tomography

The fatigue behavior of metal AM lattice structures can be significantly influenced by variations and imperfections that are typically introduced during the production process on the geometry, surface, and density of the produced part [2]. As stated in the introduction, numerical simulations are often performed on as-designed CAD geometries, with results that cannot adequately represent the actual fatigue behavior of the investigated parts. To integrate the information about the actual geometry of the analyzed lattice structures, X-ray computed tomography can be employed [33]. The capability of performing three-dimensional reconstructions of AM parts, including information on difficult-to-access regions, makes μ-CT the only technique that allows for non-destructive evaluation of parts with complex and intricate geometries such as lattice structures [34]. The inclusion of surface texture and internal defects into the 3D reconstruction, in addition to geometric details, is enabled by the use of micro-focus CT systems. Such devices can achieve high structural resolution, suitable for characterizing the surface topography as well as the internal porosity of additively manufactured metal parts [35]. Furthermore, for specific measurement tasks, metrological μ-CT systems allow for reliable dimensional measurements [36].

2.2. The Finite Cell Method: numerical analysis on μ-CT images

The geometrical models from the undamaged μ-CT scan images are difficult to analyze using standard finite element procedures. One possibility is to use voxel FEM [37]. Therein, each voxel is converted into a finite element which leads to very large models, often having billions of degrees of freedom. Another option is to convert the model into a boundary-conforming finite element mesh that can represent the as-built geometry accurately. To this end, an analysis suitable 3-dimensional finite element mesh must be generated from the μ-CT image. This poses the challenge to balance between maintaining geometric details and restrictions on the maximal aspect ratios of the finite elements. Moreover, the construction of a water-tight geometric description needs to ensure that it is an orientable two-manifold without a boundary. The Finite Cell Method (FCM) is a robust alternative to the conventional workflow as it can directly simulate on the μ-CT images, vastly simplifying the preprocessing steps necessary to prepare the μ-CT images for numerical analysis. The FCM is an immersed boundary method that employs high-order finite elements. The core principle of FCM is depicted in Fig. 1. The key idea is to extend the domain of interest Ω_{phy} (i.e. physical domain) by a fictitious domain Ω_{fic} such that the union $\Omega_{\cup} = \Omega_{phy} \cup \Omega_{fic}$ can readily be discretized with a structured mesh. Thus, boundary conforming mesh generation is replaced by directly resolving the original physical domain through numerical integration. This circumvents the restrictions posed by element-aspect ratios in mesh generation. An indicator function $\alpha(\boldsymbol{x})$ is introduced as follows:

$$\alpha(\boldsymbol{x}) = \begin{cases} 1 & \forall \boldsymbol{x} \in \Omega_{phy} \\ \epsilon = 10^{-k} \ll 1 & \forall \boldsymbol{x} \notin \Omega_{phy}. \end{cases} \tag{1}$$

The indicator function is defined to be equal to one on all points inside the physical domain Ω_{phy} and to a positive constant $\epsilon \approx 0$ for points in Ω_{fic}. Depending on the definition of the indicator function $\alpha(\boldsymbol{x})$, it is not even necessary to strictly obtain water-tight geometries. The case of a geometric model based on images obtained from μ-CT reconstructed cross-sections is especially favorable, since the indicator function $\alpha(\boldsymbol{x})$ is directly defined by the Hounsfield units HU, i.e. $\alpha(\boldsymbol{x}, HU)$, where a threshold value of the Hounsfield unit HU_{thre} is used to classify points into Ω_{phy} and Ω_{fic}.

The application of inhomogeneous boundary conditions naturally requires the definition of the surface where they are applied. Dirichlet boundary conditions can be imposed weakly by employing e.g. the penalty method or Nitsche's method, see e.g. [38] for details. Homogeneous Neumann boundary conditions require no special treatment.

The resulting modified weak formulation for a linear elasticity problem with penalty boundary conditions can be written as:

$$a(\boldsymbol{u}, \boldsymbol{v}) = f(\boldsymbol{v}) \tag{2}$$

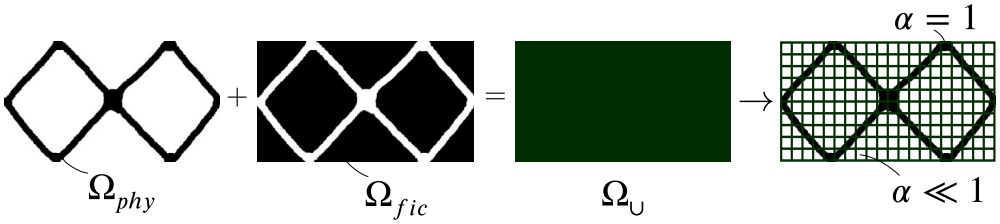

Fig. 1. The core principle of FCM: The physical domain Ω_{phy} is immersed in a readily discretizable embedding domain $\Omega_{\cup}$, where the geometry is characterized by the indicator function α.

$$a(\boldsymbol{u},\boldsymbol{v}) = \int_{\Omega_{\cup}} \varepsilon(\boldsymbol{v}) : \alpha\mathbb{C} : \varepsilon(\boldsymbol{u})\,\mathrm{d}\Omega + \int_{\Gamma_D} \beta\,\boldsymbol{v}\,\boldsymbol{u}\,\mathrm{d}\Gamma \tag{3}$$

$$f(\boldsymbol{v}) = \int_{\Omega_{\cup}} \alpha\,\boldsymbol{v}\cdot\boldsymbol{f}\,\mathrm{d}\Omega + \int_{\Gamma_D} \beta\,\boldsymbol{v}\cdot\boldsymbol{g}\,\mathrm{d}\Gamma + \int_{\Gamma_N} \boldsymbol{v}\cdot\boldsymbol{t}\,\mathrm{d}\Gamma \tag{4}$$

where ε, $\mathbb{C}$, $\boldsymbol{u}$, $\boldsymbol{v}$ and β denote the engineering strain tensor, the elastic material tensor, the unknown admissible displacements vector, the vector of admissible test functions, respectively. Additionally, $\boldsymbol{f}$, $\boldsymbol{g}$ and $\boldsymbol{t}$ represent the body forces, the prescribed Dirichlet information and the traction vector, respectively. The introduction of the indicator function results in discontinuous integrands (i.e. when a cell is cut by the boundary $\partial\Omega_{phy}$) and thus special numerical integration techniques must be employed to accurately compute the volume integrals in Eq. (3) and Eq. (4). In this contribution, the efficient technique presented in [39] is used. It is based on the observation, that in the context of the voxel-based FCM the Lamé parameters are piecewise constant within a finite cell such that the bilinear form presented in Eq. (3) can be pre-computed in a factorized manner.

Based on the solution of the initial boundary value problem defined in Eq. (2), the strain energy density at a point $\boldsymbol{x}$ within $\Omega_{\cup}$ is calculated as:

$$W(\boldsymbol{x}) = \frac{1}{2}\,\varepsilon(\boldsymbol{x}) : \alpha\mathbb{C} : \varepsilon(\boldsymbol{x}) \tag{5}$$

where the strains $\varepsilon(\boldsymbol{x})$ are computed using the strain - displacement relation. Moreover, the strain energy U_V within a control volume Ω_V can be computed as:

$$U_V = \int_{\Omega_V} W(\boldsymbol{x})\,\mathrm{d}\Omega \tag{6}$$

For further reading, refer to [15,38].

2.3. The average strain energy density approach

The numerical approach described in section 2.2 permits the evaluation of the perturbations induced on the stress field by the intrinsic metamaterial architecture and additive manufacturing-related imperfections. To evaluate their impact on the fatigue behavior of the lattice structures, we will use an average strain energy density based fatigue criterion. In its classical formulation, it postulates that a notched component is in fatigue critical condition when the ASED of the notched part $\Delta\overline{W}_{1,notch}$ equals the strain energy density (SED) in the plain sample $\Delta\overline{W}_{1,plain}$ under the same fatigue critical condition [40,41]:

$$\Delta\overline{W}_{1,notch} = \Delta\overline{W}_{1,cr} \tag{7}$$

$$\Delta\overline{W}_{1,notch} = \frac{1}{\Omega(R_1)} \int_{\Omega(R_1)} \Delta W(x)\,\mathrm{d}\Omega \tag{8}$$

$$\Delta\overline{W}_{1,plain} = \frac{1}{2E}\Delta\sigma_{cr}^2 \tag{9}$$

Where E is the Young's modulus and $\Delta\sigma_{cr}$ the full range plain fatigue limit at a given load ratio R. Ω is the control volume ahead of the notch tip where the strain energy density is averaged. Considering a problem solved with the Finite Cell Method, the strain energy density in Eq. (8) is computed thanks to Eq. (5). For plane or axisymmetric problems, the control volume simplifies into a circular domain, as schematically illustrated in Fig. 2a. Under mode I type of loading, the circular sector encompassing the notch tip is centered in the origin of the curvilinear reference frame used to describe the notch geometry and located at a distance r_0 from the notch tip moving along the notch bisector. r_0 is a function of the notch radius R and the opening angle $2\overline{\alpha}$. Consequently, the circular domain Ω has a radius $r_0 + R_1$, where R_1 is regarded as the "control radius" and is a material dependent parameter expressing its fatigue notch sensitivity. The advantages of the ASED over other notch fatigue calculation methods are widely discussed in the literature, and they can be summarized as its capacity to deal with stress singularities and in its lower mesh sensitivity [15].

A disadvantage of this approach is that the ASED loses information about the sign of the normal stresses. To discriminate the more detrimental effect of tensile with respect to compressive stresses on the fatigue strength [42,43], we will propose in section 3.1.3 to combine the criterion expressed by Eq. (9) with the hydrostatic pressure (related to the first invariant of the stress tensor), by limiting the calculation of $\Delta\overline{W}_{1,notch}$ only to those parts of the components affected by positive hydrostatic pressures.

In the present work, the size of R_1 is estimated using an inverse procedure theoretically devised in [16] and based on an optimized notched specimen geometry depicted in Fig. 2b [16]. This procedure was experimentally applied in [16] to assess R_1 for the Ti-6Al-4V ELI (Extra Low Interstitial) titanium alloy under investigation, which was fabricated by Laser Powder Bed Fusion (L-PBF) and subjected to axial fatigue testing documented in [16]. To explore the effect of defects on notch fatigue strength, two batches of samples were fabricated. The first batch, termed Turned Notch, was created by turning the notch from plain cylindrical bars. The second batch, termed L-PBF Notch, had the notch geometry introduced during the L-PBF process, followed by a slight turning finish to achieve the correct notch radius. The presence of defects of varying sizes in the two batches allowed for the estimation of the dependency of R_1 on the square root of the projected area of the critical defect, as illustrated in Fig. 2c, which reports also R_1 estimations based on the fatigue limit and the crack growth threshold values found in the literature for the wrought counterpart of the same material. Interestingly, R_1 increases with the size of the critical defect, a trend well-represented by a hyperbolic tangent function (solid line in Fig. 2c). This function will be used to assess R_1 for the material based on the μ-CT scans reported in section 3.3. The interested reader is referred to [16] for further details.

3. Materials and methods

3.1. Methodology

In this work, a methodology for image-based fatigue life estimation of lattice components is proposed. The workflow is graphically represented in Fig. 3 and is composed of three main steps: simulation of the as-built geometry, identification of the critical locations and estimation of the fatigue life.

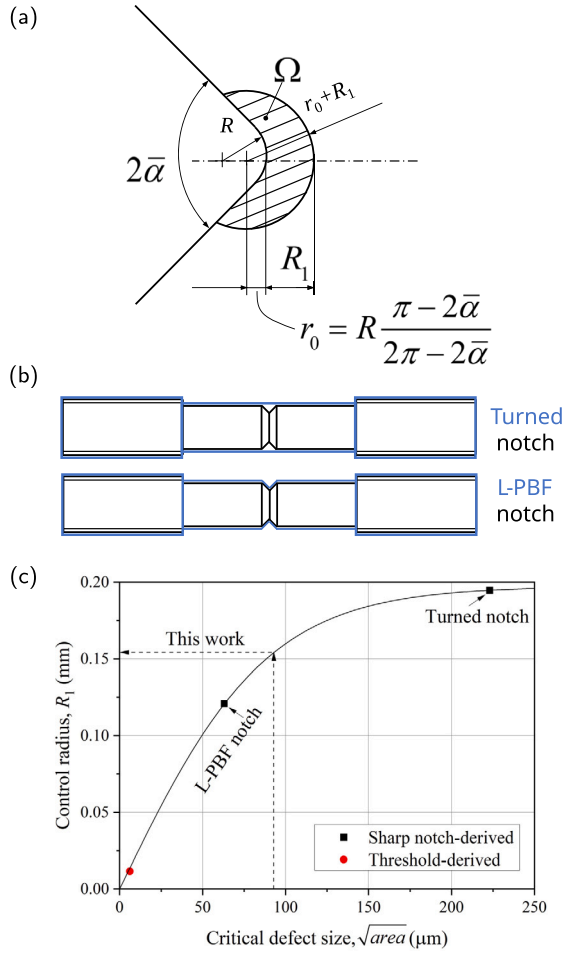

Fig. 2. (a) Strain energy density averaging domain Ω ahead of the notch root. (b) Sketch of notched specimens of Ti-6Al-4V additively manufactured and fatigue tested in [16]. Notches were fabricated directly via laser powder bed fusion (L-PBF notch) or by turning additively manufactured cylindrical bars (Turned notch). (c) Control radius dependency upon the critical defect size from experimental data collected in [16] for additively manufactured Ti-6Al-4V and from the literature for a conventionally processed material with similar microstructure. The dotted line represents the control radius R_1 considered in this study as discussed in section 3.1.2.

3.1.1. Simulation on as-built geometries

Initially, the lattice component geometry is defined in a computer-aided design (CAD) software and subsequently manufactured using metal powder bed fusion techniques. After production, a μ-CT scan of the undamaged part is performed to obtain the as-built geometry, including manufacturing-induced defects such as partially melted particles attached onto the lattice structure's surfaces and internal pores. The as-built geometry is directly simulated using the image-based Finite Cell Method [1]. This technique is employed to accurately compute the elasto-static behavior of the as-built geometry under a specified load, and it is selected to leverage its computational efficiency in simulating complex as-built geometries.

3.1.2. Critical location identification

After the simulation, the identification of the locations prone to fatigue failure has to be addressed. To this end, the average strain energy density method is employed. This technique requires the identification of locations with high strain energy in the analyzed component and compares the energetic state to the one computed on bulk unnotched specimens under uniaxial loading. Three hypotheses are considered in the analysis of lattice specimens: firstly, the loading conditions of the lattice specimens promote the failure by mode I, i.e. tensile loading, secondly, the stress intensification locations generated by the presence of partially melted particles on the specimen surface are considered to be sharp notches; for this reason, the radius r_0 in Fig. 2a is set equal to 0 and the selection radius is centered at the stress peak. Lastly the critical radius, R_1, is used to select a spherical region in the 3D lattice geometry. The control radius R_1 is a material property and considers the AM nature of the component. As discussed in section 2, this quantity is sensitive to the material porosity, and requires the knowledge of the average defect area $\sqrt{area}$. The average dimension in the lattice structure is considered as in [18], since it is assumed to be representative of the maximum defect expected in the control region determined by R_1. The pore dimension is available thanks to the μ-CT analysis, and a visual example of R_1 estimation is provided in Fig. 8.

To identify critical regions within the lattice structure, the nodes associated with the highest values of the Von Mises stress, σ_p are considered, and the locations of the stress peaks are used as a marker denoting regions prone to crack nucleation and propagation. As stated, this region is defined as a sphere, and the average strain energy density is computed as the average of all the strain energy density values within it. The radius of the sphere is the critical radius R_1 obtained through the analysis of internal material defects. Once the most critical point is analyzed, the elements in the associated critical radius are removed and the remaining part of the specimen is considered. Thus, the identification of the critical locations is an iterative process which is given in Algorithm 1.

Algorithm 1 Critical Location Identification.

```
Start
repeat
    Find location x_p with peak Von Mises stress σ_p
    Create a control volume at x_p with radius R_1.
    if σ_hydrostatic,p ≥ 0 then
        Compute ASED averaging SED over the volume
    end if
    Deselect the sphere from the model
until σ_p < σ_*
Stop
```

Only the stress peaks associated with a tensile condition are considered critical for the fatigue life [42,43]. For this reason, the hydrostatic pressure $\sigma_{hydrostatic,p}$ of each critical point is computed and the location is considered critical and kept in the analysis if the hydrostatic pressure is positive and, thus, associated to a tensile state.

The iterative procedure continues until the stress peak (σ_p) is no longer considered critical. The determination of σ_p typically depends on the material's strength and the loading conditions of the component. While it is theoretically possible to fully extract the component's stress state, such an approach is linked to significant computational costs. To address this issue, a threshold, σ_* is set to the minimum fatigue strength measured on miniaturized strut-junction specimens at the fatigue limit. These specimens are used to understand the fatigue resistance of lattice structures by measuring the fatigue properties of their sub-unital elements [42].

3.1.3. Fatigue life estimation

Once the critical locations have been identified, statistics of extrema is employed to investigate which locations are the most critical and likely to induce fatigue failure. The average strain energy density of the population is considered, and a peak over threshold approach is applied. The distribution of ASED is computed and fitted with a generalized Pareto distribution (GPD) using the Maximum Likelihood method as follows:

$$GDP(x) = 1 - \left(1 + \gamma\left(\frac{x-\lambda}{\delta}\right)\right)^{-\frac{1}{\gamma}} \tag{10}$$

In accordance with [44], the threshold is computed using the mean excess method, selecting the point in the mean excess plot where the data

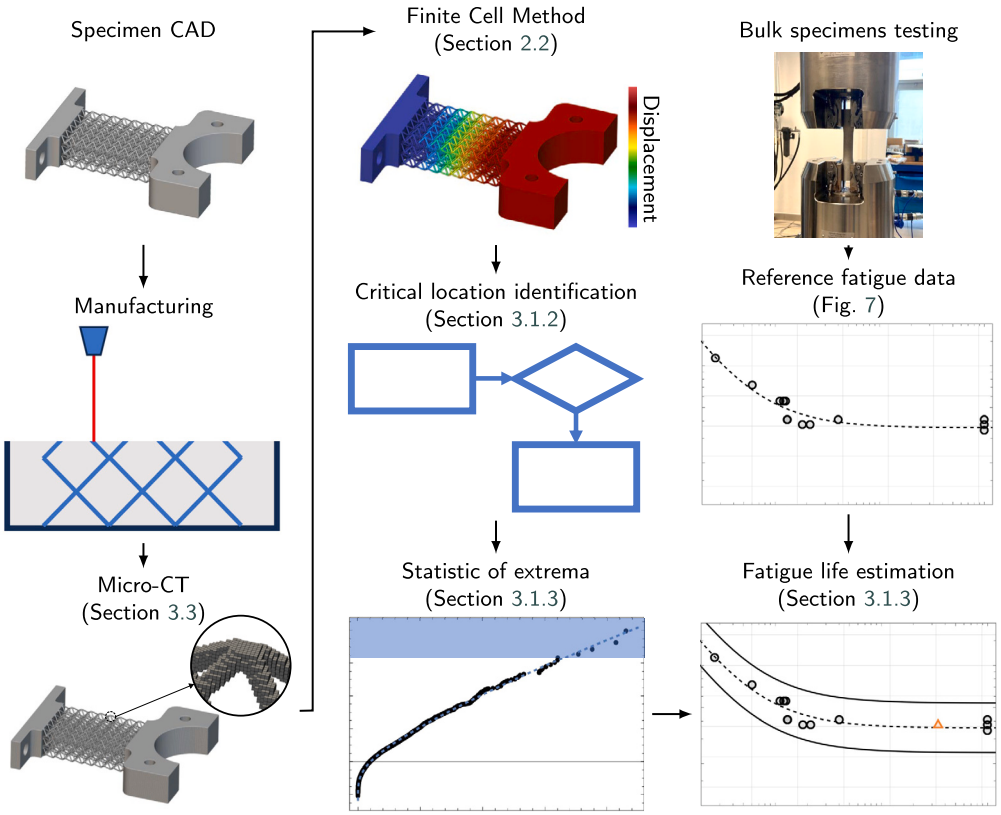

Fig. 3. Workflow for the determination of lattice structure's fatigue life estimation. The as-built geometry is analyzed through μ-CT-scan analysis and the strain distribution is computed with the Finite Cell Method. Through the usage of Algorithm 1 and subsequently the procedure depicted in Fig. 4, the critical locations of the structure are identified. The most critical locations are compared to the experimental data obtained from bulk unnotched specimens to predict component fatigue life.

can be approximated by a line. A visual representation of this workflow is depicted in Fig. 4. Based on this distribution, a selection of the most critical locations is performed: the ASED associated with the 99% probabilities of the GPD is computed. Values above this threshold identify the 1% most critical locations in the structure. Among this set, the average value of the ASED is computed to identify the critical ASED associated with this threshold.

The identified critical locations are the most likely to promote crack growth and lead to component fatigue failure. To estimate the fatigue resistance of the analyzed component, the average value of the ASED can be compared with the experimental bulk reference curve.

3.2. Lattice structure specimens

To validate the proposed method, this study leverages data from a previous work [5] that investigated the optimal printing orientation for lattice structures to enhance fatigue resistance. The research focused on a three-point bending lattice specimen featuring an Octet Truss (OT) cell topology, as shown in Fig. 5. Each lattice cell had dimensions of 3 mm with a strut diameter of 0.7 mm, resulting in a lattice porosity of 48%. The specimen, depicted in Fig. 6, consisted of an $4 \times 20 \times 2$ array of OT cells, measuring 12 mm$\times$60 mm$\times$6 mm. Two batches of specimens were fabricated using Ti6Al4V biomedical grade powder via Laser Powder Bed Fusion (L-PBF) and subjected to compressive-compressive fatigue testing with a load ratio of $R = 0.1$. The "control" batch consisted of specimens printed with a standard orientation aimed at minimizing support structures, while the "optimized" batch included specimens printed with an orientation recommended by an optimization algorithm. One specimen from each batch, designated as "A" for the control batch and "B" for the optimized batch, was selected for in-depth analysis. Fig. 6a illustrates the core concept from [5], while Fig. 6b

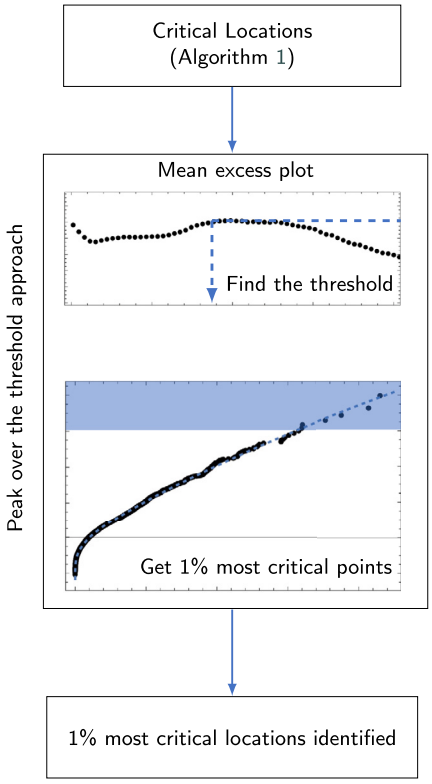

Fig. 4. Statistical tools used to determine the 1% most critical locations in the lattice structure.

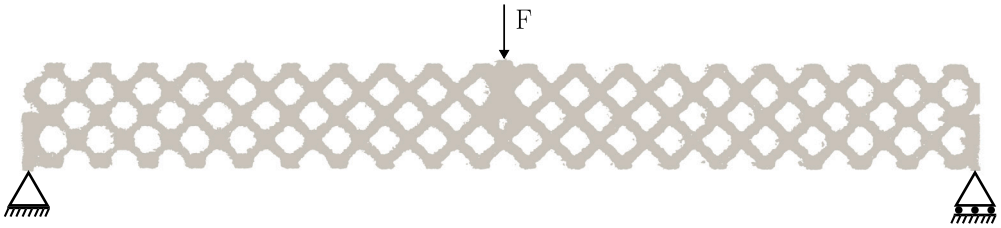

Fig. 5. A sketch, in 2D, of a three-point bending setup (adapted from [1]).

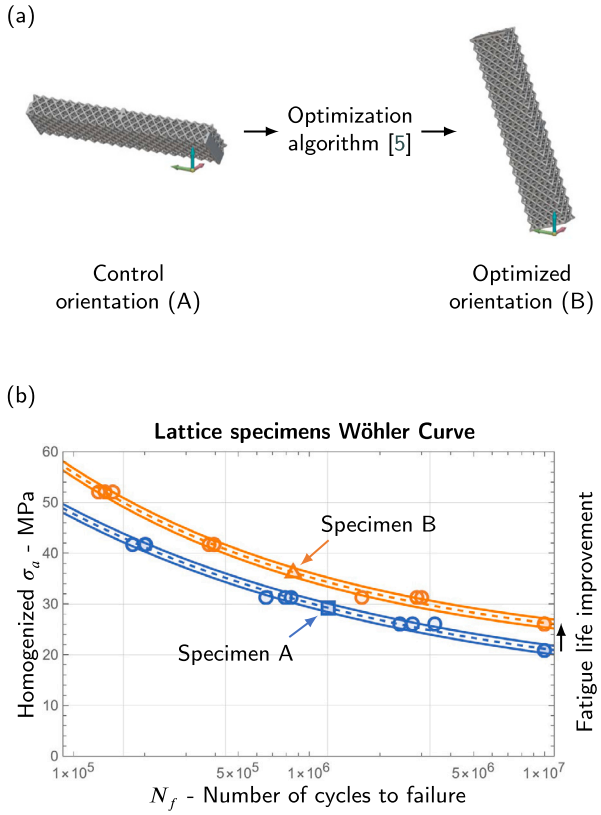

Fig. 6. (a) General concept presented in [5], where the orientation of the lattice structure in the printing chamber is optimized to improve the fatigue life. (b) Experimental results for the control and optimized batches with the indication of specimens A and B which underwent μ-CT-scan analysis.

presents the experimental outcomes along with the definitions of specimens "A" and "B".

Within this broader context, this contribution focuses on fatigue life estimation by exclusively analyzing specimens A and B. These specimens underwent detailed analysis using metrological μ-CT before and after fatigue testing to investigate internal structural integrity and failure mechanisms.

3.3. Micro-CT analyses

Specimens A and B underwent μ-CT scanning using a metrological CT system (Nikon Metrology MCT225), characterized by a micro-focus X-ray tube with a minimum focal spot size equal to 3 µm, a 16-bit flat-panel detector with 2000 × 2000 pixels, and a shielding cabinet with controlled temperature at 20 ± 0.5 °C. 3000 bi-directional projections were acquired with the following settings: X-ray tube voltage at 190 kV, filament current at 36 μA, 2 seconds of exposure, with 1 frame per projection and a 0.25 mm-thin copper physical filter, which was interposed between the tube's target and the scanned lattice structure to reduce the beam hardening effect. In order to achieve a voxel size suited to reconstruct surface features and internal pores in the micro-scale range, μ-CT scans were conducted on four different regions of each specimen. Each region measures approximately 12 mm × 15 mm × 6 mm. The μ-CT images of the four regions were later combined into one unified image per specimen. An overlapping portion was kept between adjacent regions to aid the subsequent registration of the reconstructed regions. A voxel size of 13 µm was obtained through this approach. 3D reconstructions were conducted using the CTPro 3D software provided by Nikon Metrology. The registration of regions was addressed in the software VGStudio MAX (Volume Graphics GmbH) by a manual pre-alignment followed by a refined best-fit alignment leveraging the overlapping regions and considering the pre-alignment as a positional constraint. Cross-sections of the entire lattice structures (A and B) were then exported as image stacks to be further elaborated as described in section 3.4. Porosity analyses were conducted directly on 3D reconstructions using the Porosity module available in VGStudio MAX. The location of cracks induced by fatigue testing (see section 4.4) was eventually evaluated by repeating the measurement procedure described above on the same specimens (A and B) after fatigue testing.

3.4. Finite Cell model and critical location extraction

The segmentation of the μ-CT images is carried out to determine Ω_{phy} and Ω_{fic}. The indicator function $\alpha(\boldsymbol{x})$ is then defined following Eq. (1). The segmented geometries of specimen A and B are directly used in the context of the FCM, as described in section 2.2, to simulate a quasi-static three-point bending test illustrated in Fig. 5. The load case and boundary conditions closely follow the experimental setting in [5], such that resultant forces of 140 N and 175 N are uniformly distributed over the load surface of specimen A and B, respectively.

Once the finite cell simulations are complete, the methodology described in section 3.1.2 is applied. The critical locations are identified based on the procedure depicted in Algorithm 1, where a threshold value of $\sigma_* = 35$ MPa is set. This corresponds to the minimum fatigue strength for miniaturized strut-junction specimens at the fatigue limit, as reported in [5]. The population of critical locations is then analyzed with the Peak over Threshold method as described in section 3.1.3 and visually reported in Fig. 4.

To estimate the fatigue life of the lattice component, a reference for the fatigue resistance must be provided. Consistent with the lattice tested, data from bulk unnotched specimens manufactured with the L-PBF technique in Ti6Al4V, as published in [32] and shown in Fig. 7, are used. These tests were conducted under tension-tension loading conditions with a stress ratio $R = 0.1$. The average strain energy density (ΔW) can be computed from the fatigue curve using the Eq. (9). For this analysis, a typical value of $E = 110$ GPa is selected for the Ti6Al4V components.

4. Results and discussion

4.1. Average strain energy density criterion parameters

Given the experimental data presented in [32], Eq. (9) is applied to compute the critical SED for bulk unnotched specimens. The reference curve obtained with this procedure is depicted in Fig. 7. For each of

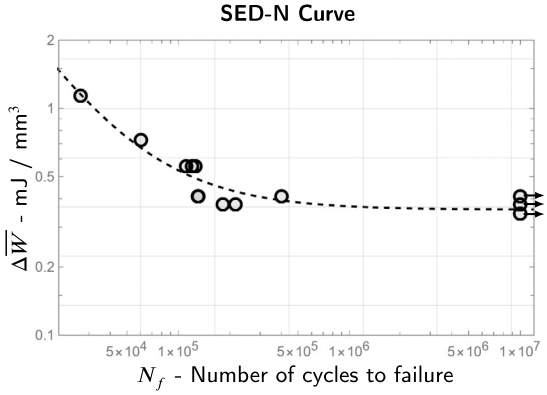

Fig. 7. Reference SED-N curve generated with experimental data from [32]. Data marked with an arrow indicate a runned-out specimen.

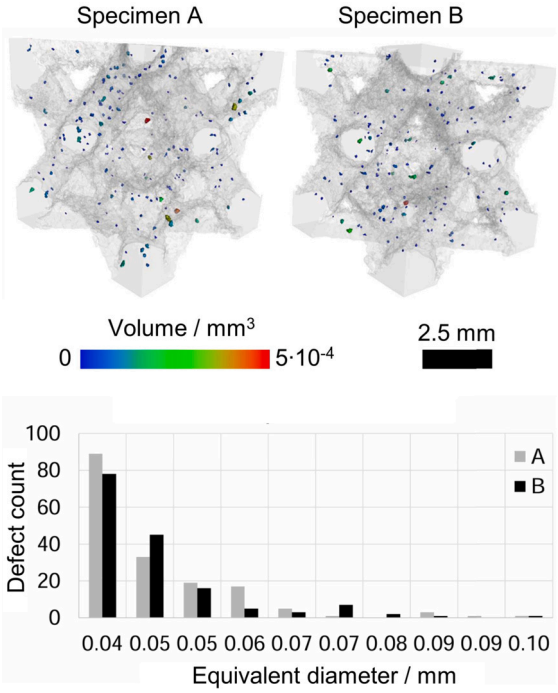

Fig. 8. μ-CT reconstructed regions of interest of specimens A and B, showing the internal porosity distribution and volume (above), and distribution of equivalent diameters of pores measured by μ-CT for specimens A and B (below).

the two specimens (A and B), μ-CT scans are used to analyze internal defects, as explained in section 3.3. For each identified pore, the volume is measured, and from this, the equivalent pore radius is derived. The criticality of the average defect is expressed in terms of the square root of the area, as prescribed by [32]. The results obtained are as follows: for specimen A, the average $\sqrt{area}$ of the defect is 88.17 µm, while for specimen B, it is 95.16 µm. A graphical representation of the defect distribution is depicted in Fig. 8a.

This analysis provides the required input to compute the critical radius, R_1. According to the chart published by [32] and presented in Fig. 2c, the two specimens are described by $R_1 = 0.152$ mm. The computation of the average strain energy density values using the FCM is performed according to this radius.

4.2. Numerical analysis of three-point bending specimens

The numerical analysis of the three-point bending specimens A and B are carried out by using the FCM as introduced in section 2.2. The constant ϵ penalizing the fictitious domain is chosen as 10^{-9}. Then, the segmented μ-CT-images of specimens A and B are embedded into a finite cell mesh with a polynomial degree $p = 2$, where each cell contains $8\times8\times8$ voxels. Consequently, a total of $148\times606\times98$ and $142\times602\times92$ cells are used for specimens A and B, respectively. The discretization used for specimen B is depicted in Fig. 9. The resulting displacements and strain energy densities are depicted in Fig. 10. The corresponding results for specimen A can be found in the Appendix. All computations are carried out on four compute nodes, where each node has a total of 80 physical cores and 767 GB of random-access memory (RAM). The wall-clock time of the μ-CT-image based FCM analyses are 8 hours 22 minutes and 9 hours 20 minutes for specimen A and B, respectively.[2] Note that a relatively coarse mesh size is selected based on the observation that the averaged strain energy density parameter, calculated following Algorithm 1, can be computed with sufficient resolution without a relatively fine mesh [40]. One possible rationale for this observation is the smoothing effect of averaging the SED values over a control volume, which in this case has a diameter of more than 20 voxels. In general, however, a voxel resolution of $4\times4\times4$ or $2\times2\times2$ is better suited to analyze stress states, especially in the vicinity of small features.

4.3. Statistical analysis

Once the simulation is completed, the results can be analyzed statistically through the method presented in section 3.4. The threshold for ASED data is computed using the mean excess method, selecting the point in the mean excess plot Fig. 11a where the data can be approximated by a line, so from $\Delta W^* = 0.1\,\mathrm{mJ/mm^3}$ onward. A common threshold of $\Delta W^* = 0.1\,\mathrm{mJ/mm^3}$ is selected for both specimens A and B. The selected threshold is a better fit for specimen A, and for the sake of consistency, the same threshold is defined for specimen B. The data distribution is depicted in Fig. 11b, while the GDP formulation is reported in Eq. (10). Based on this distribution, the ASED associated with the 99% probability are identified and the average value of the ASED is computed.

4.4. Fatigue life estimation

The ASED values associated with the 1% most critical locations in the structure are averaged and compared with the critical average strain energy density obtained from experimental data for bulk unnotched specimens, as reported in section 3.1. Both specimens A and B are analyzed according to this procedure, and the average ASED values are represented in the SED-N chart associated with the experimental number of cycles that lead the specimens to failure. The comparison is illustrated in Fig. 12, where uncertainty bars associated with a factor of ±1.5 are depicted. In accordance with [46], the factor of ±1.5 corresponds to an error band of approximately $\pm22\%$ on the stress amplitude.

The comparison shows an excellent agreement between the points associated with the 1% most critical ASED values and the experimental results. A comparative in-depth analysis is performed by comparing the crack locations detected in the μ-CT reconstructions acquired after the fatigue test with the critical locations identified in the finite cell simulation. The characteristics of the critical locations are reported in Table 1.

4.5. Experimental failure location and simulated critical location comparison

The set identified in the statistical analysis containing the 1% most critical locations is overlapped with the specimens' geometries to inves-

[2] The implementation of image-based FCM used for this study has favorable parallel scaling characteristics such that increasing the number of compute nodes provides almost-linear speed-up [45]. Thus, a relatively small high performance (HPC) cluster with 50 compute nodes can offer wall-clock times that are under an hour per analysis.

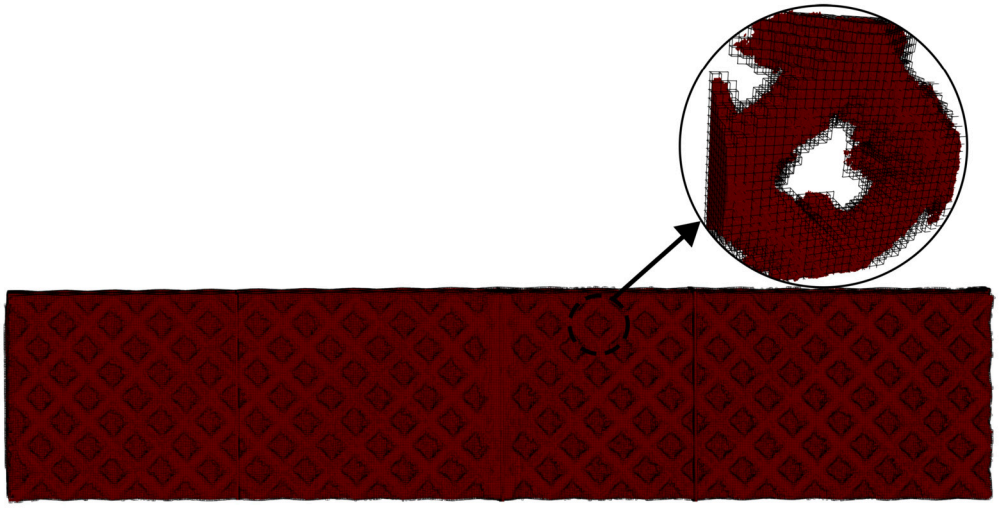

Fig. 9. The finite cell mesh of the specimen B, based on the as-built geometry from the μ-CT.

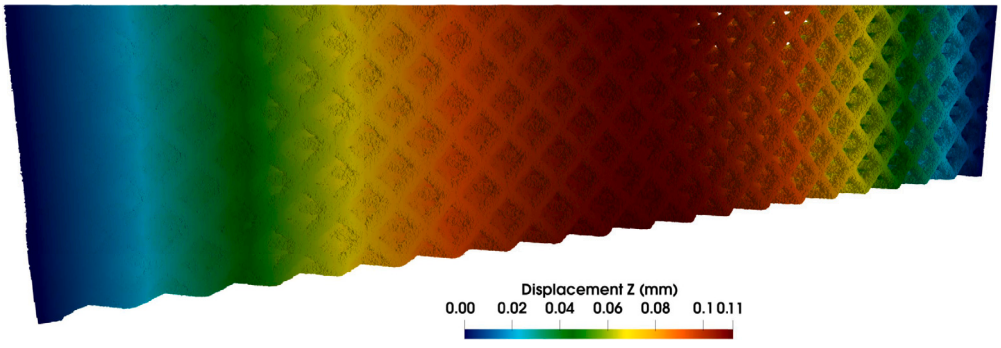

(a) The displacement field in the direction of the load

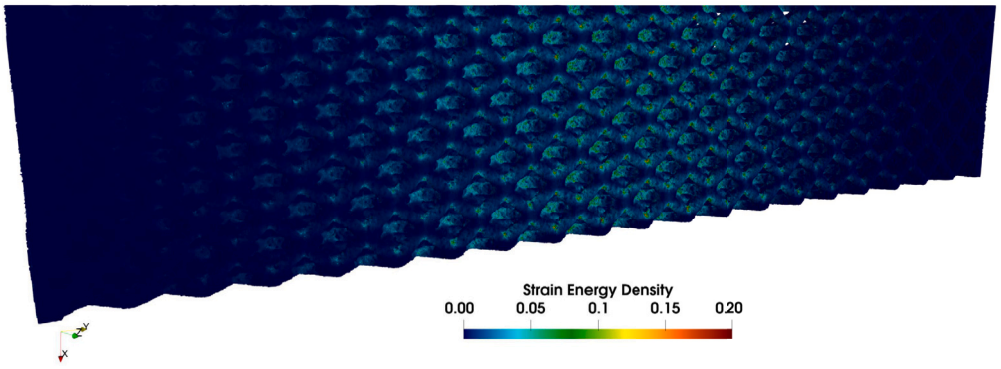

(b) The distribution of the strain energy density

Fig. 10. The μ-CT-image based FCM analysis on the specimen B: the displacement and strain energy density fields.

Table 1
Characteristics of the 1% set of most critical points in the specimens A and B.

Spec.	1% most critical points $\Delta\overline{W}$ - mJ/mm^3	Number of points
A	0.276	10
B	0.382	29

tigate the position of the detected critical volumes. For both specimens A and B, all the most critical locations are found in the lowermost layer of cells near the symmetry plane. This outcome is easily justified, as these locations are subjected to the highest tensile loads in a homogenized three-point bending condition. Considering the lattice structure topology, the critical locations are identified near lattice nodes. This is a realistic result, given the stress intensification generated by the convergence of the different struts in the nodes. Moreover, the critical locations are identified to coincide with the geometrical imperfections captured by the μ-CT analysis of partially melted particles attached onto the lattice structures surfaces. These surface patterns are typical of the as-built state and they act as stress raisers, resulting in struts with high-energy locations that are prone to the nucleation and propagation of fatigue cracks. The ORS-Dragonfly (Comet Technologies Canada Inc, Canada) software was used to visually inspect the μ-CT data obtained after fa-

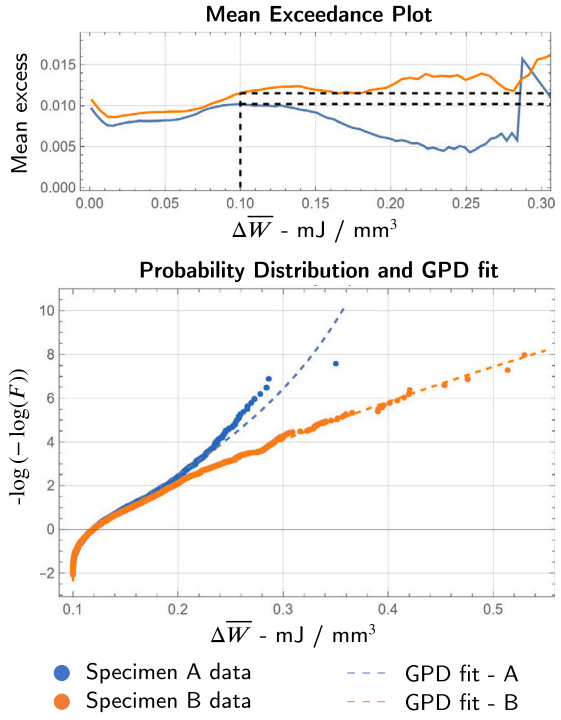

Fig. 11. (a) Mean excess plot for average strain energy density data for specimens A and B. (b) Probability distributions and Generalized Pareto Distributions best fitting the experimental data for the two specimens under investigation.

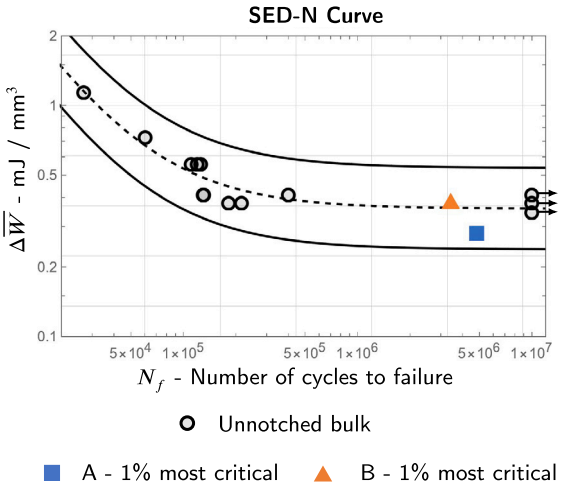

Fig. 12. Predicted average ASED values for specimens A and B displayed on the experimental number of cycles to failure with respect to the experimental data presented in Fig. 7. Uncertainty bars are associated with an error of ±22% on the $\Delta\sigma$.

tigue testing and analyze the effect of the fatigue loading, with a focus on identifying fatigue cracks. The fatigue cracks are predominantly located in the lowermost level of struts near the symmetry plane, which aligns with the critical locations characterized by maximum tensile stress identified in the numerical simulation. Analyzing μ-CT data, it is noted that experimental cracks are mainly situated near the lattice nodes and developing from surface manufacturing-induced defects, such as partially melted powder particles. Understanding the genesis of these cracks is complex with the information provided by μ-CT-scan; however, the presence of manufacturing-induced defects at the crack locations indicates a causal relationship. A comparative analysis of the identified 1% most critical locations for specimens A and B and the crack locations from the post-test μ-CT scans is depicted in Fig. 13. The critical locations identified by the average strain energy density computed via the Finite Cell Method are concentrated near the experimentally observed crack locations. Some of these identified locations directly overlap with the fatigue cracks, demonstrating the method's capability to statistically predict critical locations in lattice components. Improving accuracy will require more advanced techniques, such as higher-resolution μ-CT scans and finer computational meshes. The presented methodology might also benefit from taking the local Young's module into account, as carried out e.g. in [24] to compute the stress–strain response of laser powder bed fusion lattice structures. Additionally, more complex material models that capture the stages of crack formation can be considered. However, developing such models is a challenging task due to the significant computational resources required.

Experimental cracks are also identified in locations where the numerical method do not predict critical points. This discrepancy can be explained by considering the time evolution of failure propagation along the specimens. Fatigue tests were halted when a change in resonance frequency was detected [5]. This threshold was set to ensure the presence of at least one fatigue crack in the tested specimens. The formation of an initial crack weakens the affected strut, eventually causing its failure. This changes the lattice structure's topology and redistributes the load among the remaining struts, creating a new stress state and leading to the emergence of new critical locations [47]. In the presented methodology however, only the initial component geometry is considered. Therefore, only the most critical locations for the first crack nucleation are predicted.

5. Conclusions

In this work, a novel methodology for an accurate prediction of the fatigue life of metal additive manufacturing metamaterials is described. This method is founded on three technical and technological pillars: the usage of μ-CT scan to reconstruct the three-dimensional specimen's as-built geometry, the image-based finite cell simulation and the usage of the average strain energy density criterion. A validation of the method is presented, demonstrating the consistency of the simulation results with the experimental data and suggesting the suitability of the method for predicting fatigue behavior in lattice structures. The power of the method in identifying the most critical locations in the lattice structure is validated, comparing the critical locations identified by the numerical method and the experimental fatigue crack. A solid agreement is found, where the statistically predicted locations of failure match the specimens' critical areas characterized by experimental cracks. The concurrent application of the finite cell method on μ-CT reconstructed geometries and strain energy density criterion is shown to be a novel and powerful tool to predict fatigue resistance and crack-prone locations in lattice structures.

The presented results serve as a proof of concept, demonstrating the applicability of the method for the considered case study. Future developments require the analysis of a larger experimental campaign to extensively test the proposed method on different lattice topologies, porosities, materials and load cases.

CRediT authorship contribution statement

Raffaele De Biasi: Writing – review & editing, Writing – original draft, Visualization, Validation, Software, Resources, Methodology, Investigation, Formal analysis, Conceptualization. **Oguz Oztoprak:** Writing – review & editing, Writing – original draft, Visualization, Validation, Software, Resources, Methodology, Investigation, Formal analysis, Data curation, Conceptualization. **Filippo Zanini:** Writing – review & editing, Writing – original draft, Investigation, Data curation. **Simone Carmignato:** Writing – review & editing, Writing – original draft, Supervision, Investigation, Data curation. **Stefan Kollmannsberger:** Methodology, Writing – review & editing, Supervision, Project administration,

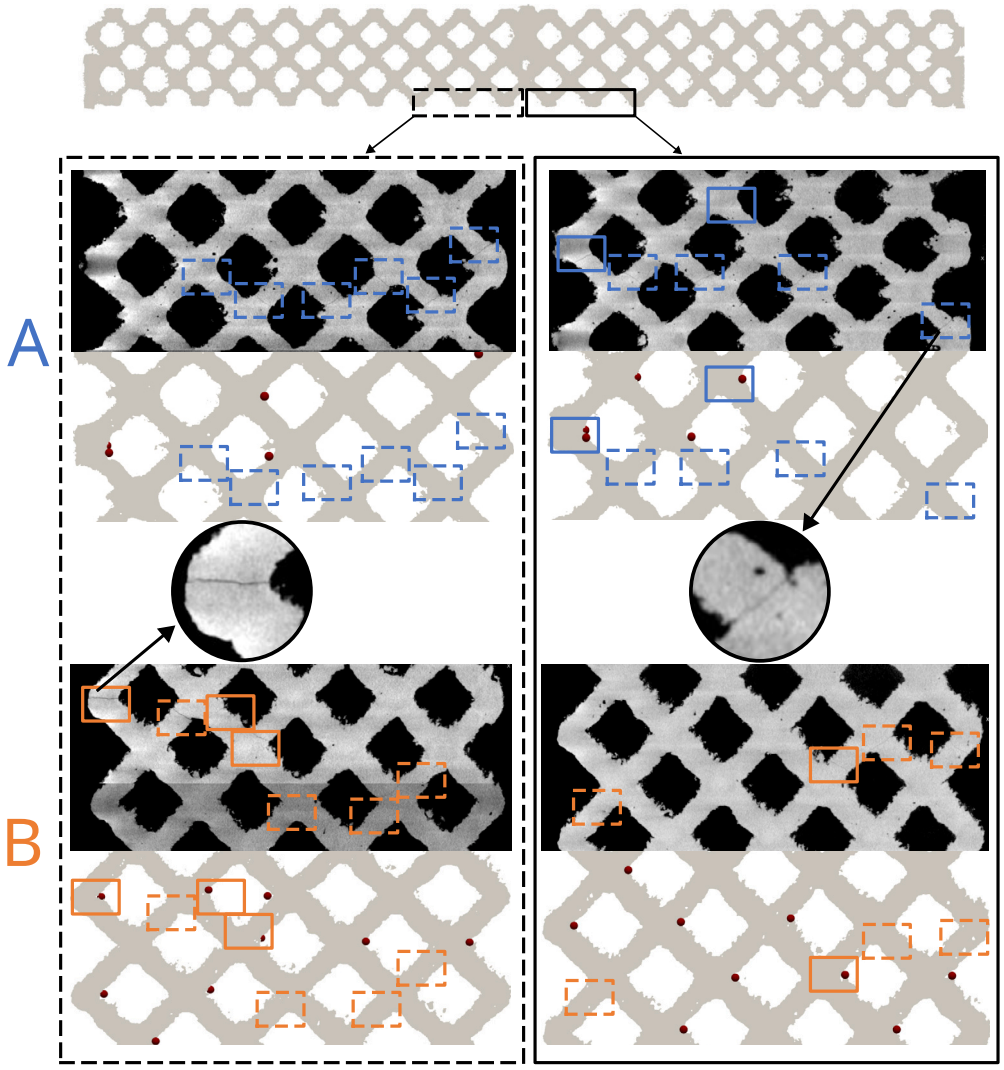

Fig. 13. A visual comparison between the experimental crack locations of specimens A and B, as acquired by the μ-CTs after the fatigue test, and the 1% most critical locations as determined following section 3.1.2. The solid blue and orange rectangles illustrate the positions where the crack locations and critical points are in a good agreement for specimen A and B, respectively. The dashed blue and orange rectangles show the areas where there is a visual crack without a corresponding critical location.

Funding acquisition, Conceptualization. **Matteo Benedetti:** Writing – review & editing, Writing – original draft, Supervision, Project administration, Methodology, Funding acquisition, Conceptualization.

Declaration of competing interest

The authors declare the following financial interests/personal relationships which may be considered as potential competing interests: Oguz Oztoprak reports financial support was provided by German Research Foundation. Stefan Kollmannsberger reports financial support was provided by German Research Foundation. If there are other authors, they declare that they have no known competing financial interests or personal relationships that could have appeared to influence the work reported in this paper.

Data availability

All data is available under DOI https://doi.org/10.14459/2024mp1751465, see [48].

Declaration of generative AI and AI-assisted technologies in the writing process

During the preparation of this work the authors used ChatGPT (based on GPT-4 - OpenAI) in order to reorganize the notes and improve the manuscript readability. After using this tool/service, the authors reviewed and edited the content as needed and take full responsibility for the content of the published article.

Acknowledgements

The authors would like to thank Simone Murchio, Matteo Pedranz, Lorena Emanuelli, and Sunil Raghavendra of the University of Trento for their kindness and availability in discussing the presented topics.

This research was funded by the Deutsche Forschungsgemeinschaft (DFG, German Research Foundation)—project number 414265976—TRR 277, C01.

Appendix A. Analysis results for specimen A

See Fig. 14.

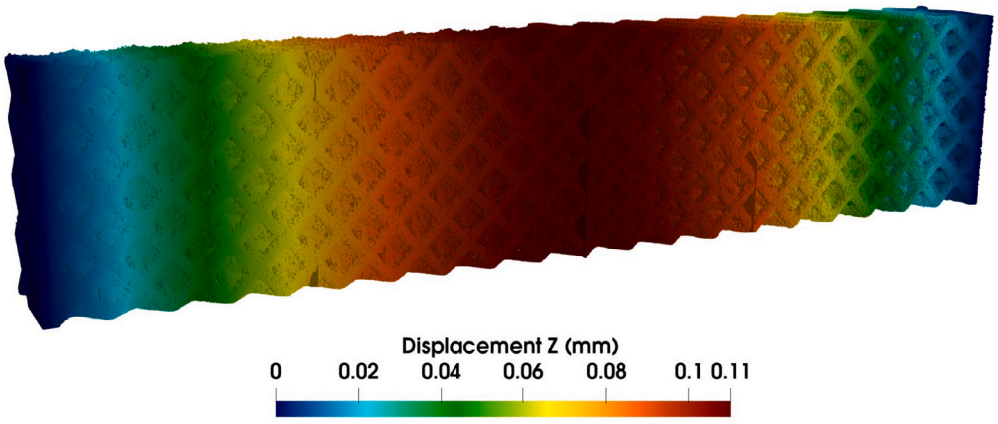

(a) The displacement field in the direction of the load

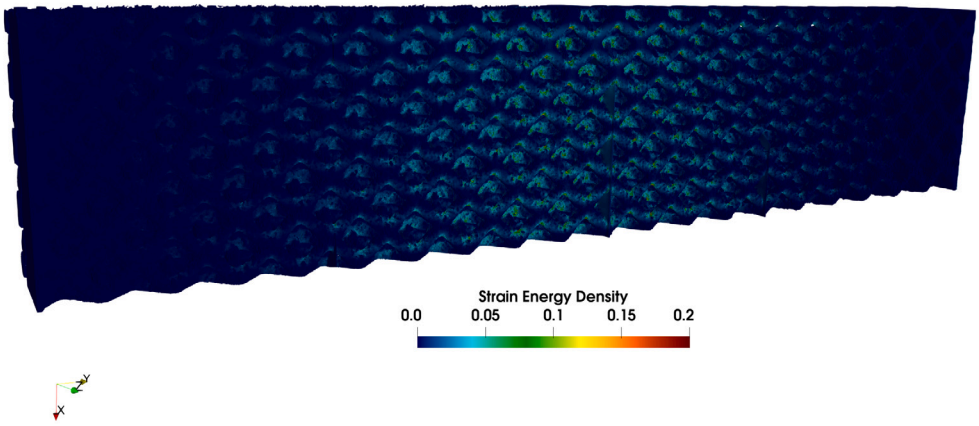

(b) The distribution of the strain energy density

Fig. 14. The μ-CT-image based FCM analysis on the specimen A: the displacement and strain energy density fields.

References

[1] N. Korshunova, G. Alaimo, S.B. Hosseini, M. Carraturo, A. Reali, J. Niiranen, F. Auricchio, E. Rank, S. Kollmannsberger, Bending behavior of octet-truss lattice structures: modelling options, numerical characterization and experimental validation, Mater. Des. 205 (2021) 109693.

[2] Niloofar Sanaei, Ali Fatemi, Defects in additive manufactured metals and their effect on fatigue performance: a state-of-the-art review, Prog. Mater. Sci. 117 (2021) 100724.

[3] S. Leuders, M. Thöne, A. Riemer, T. Niendorf, T. Tröster, H.A. Richard, H.J. Maier, On the mechanical behaviour of titanium alloy TiAl6V4 manufactured by selective laser melting: fatigue resistance and crack growth performance, Int. J. Fatigue 48 (2013) 300–307.

[4] S. Tammas-Williams, P.J. Withers, I. Todd, P.B. Prangnell, The influence of porosity on fatigue crack initiation in additively manufactured titanium components, Sci. Rep. 7 (1) (2017) 7308.

[5] R. De Biasi, S. Murchio, E. Sbettega, S. Carmignato, V. Luchin, M. Benedetti, Efficient optimization framework for l-pbf fatigue enhanced ti6al4v lattice component, Mater. Des. 230 (2023).

[6] Pietro Foti, Nima Razavi, Ali Fatemi, Filippo Berto, Multiaxial fatigue of additively manufactured metallic components: a review of the failure mechanisms and fatigue life prediction methodologies, Prog. Mater. Sci. 137 (2023) 101126.

[7] G. Sines, J.L. Waisman, T.J. Dolan, in: George Sines, J.L. Waisman, J. Dolan, et al. (Eds.), Metal Fatigue, in: University of California Engineering Extension Series, McGraw-Hill, 1959.

[8] Luca Susmel, David Taylor, The Theory of Critical Distances as an alternative experimental strategy for the determination of KIc and ΔKth, Eng. Fract. Mech. 77 (9) (2010) 1492–1501.

[9] L. Boniotti, S. Beretta, L. Patriarca, L. Rigoni, S. Foletti, Experimental and numerical investigation on compressive fatigue strength of lattice structures of AlSi7Mg manufactured by SLM, Int. J. Fatigue 128 (2019) 105181.

[10] L. Boniotti, S. Dancette, M. Gavazzoni, J. Lachambre, J.Y. Buffiere, S. Foletti, Experimental and numerical investigation on fatigue damage in micro-lattice materials by Digital Volume Correlation and μ CT-based finite element models, Eng. Fract. Mech. 266 (2022) 108370.

[11] B. Crossland, Effect of large hydrostatic pressures on the torsional fatigue strength of an alloy steel, Proc. Int. Conf. Fatig. Metals 138 (1956).

[12] D.J. Burns, J.S.C. Parry, Effect of large hydrostatic pressures on the torsional fatigue strength of two steels, J. Mech. Eng. Sci. 6 (3) (1964) 293–310.

[13] Gianluca Alaimo, Massimo Carraturo, Nina Korshunova, Stefan Kollmannsberger, Numerical evaluation of high cycle fatigue life for additively manufactured stainless steel 316L lattice structures: preliminary considerations, Mater. Des. Process. Commun. 3 (4) (2021).

[14] Antonio Coluccia, Giorgio De Pasquale, Strain-based method for fatigue failure prediction of additively manufactured lattice structures, Sci. Rep. 13 (2023) 22775.

[15] F. Berto, P. Lazzarin, Recent developments in brittle and quasi-brittle failure assessment of engineering materials by means of local approaches, Mater. Sci. Eng., R Rep. 75 (2014) 1–48.

[16] M. Benedetti, M. Dallago, C. Santus, Statistical significance of notch fatigue prognoses based on the strain-energy–density method: application to conventionally and additively manufactured materials, Theor. Appl. Fract. Mech. 109 (2020) 102720.

[17] Rolf-Dieter Reiss, Michael Thomas, Statistical Analysis of Extreme Values, Birkhäuser, Basel, 1997.

[18] S. Raghavendra, M. Dallago, F. Zanini, S. Carmignato, F. Berto, M. Benedetti, A probabilistic average strain energy density approach to assess the fatigue strength of additively manufactured cellular lattice materials, Int. J. Fatigue 172 (2023) 107601.

[19] Alomar Zaki, Franco Concli, A review of the selective laser melting lattice structures and their numerical models, Adv. Eng. Mater. 22 (12) (2020) 2000611.

[20] Lu Liu, Paul Kamm, Francisco García-Moreno, John Banhart, Damiano Pasini, Elastic and failure response of imperfect three-dimensional metallic lattices: the role of geometric defects induced by Selective Laser Melting, J. Mech. Phys. Solids 107 (2017) 160–184.
[21] Xiaofei Cao, Yongbo Jiang, Tian Zhao, Panding Wang, Yongzhen Wang, Zihao Chen, Ying Li, Dengbao Xiao, Daining Fang, Compression experiment and numerical evaluation on mechanical responses of the lattice structures with stochastic geometric defects originated from additive-manufacturing, Composites, Part B, Eng. 194 (2020) 108030.
[22] Bill Lozanovski, Martin Leary, Phuong Tran, Darpan Shidid, Ma Qian, Peter Choong, Milan Brandt, Computational modelling of strut defects in SLM manufactured lattice structures, Mater. Des. 171 (2019) 107671.
[23] Bill Lozanovski, David Downing, Phuong Tran, Darpan Shidid, Ma Qian, Peter Choong, Milan Brandt, Martin Leary, A Monte Carlo simulation-based approach to realistic modelling of additively manufactured lattice structures, Addit. Manuf. 32 (2020) 101092.
[24] Pietro Magarò, Gianluca Alaimo, Massimo Carraturo, Emanuele Sgambitterra, Carmine Maletta, A novel methodology for the prediction of the stress–strain response of laser powder bed fusion lattice structure based on a multi-scale approach, Mater. Sci. Eng. A 863 (2023) 144526.
[25] M. Dallago, S. Raghavendra, V. Luchin, G. Zappini, D. Pasini, M. Benedetti, Geometric assessment of lattice materials built via Selective Laser Melting, Mater. Today Proc. 7 (2019) 353–361.
[26] Bill Lozanovski, David Downing, Rance Tino, Anton Du Plessis, Phuong Tran, John Jakeman, Darpan Shidid, Claus Emmelmann, Ma Qian, Peter Choong, Milan Brandt, Martin Leary, Non-destructive simulation of node defects in additively manufactured lattice structures, Addit. Manuf. 36 (2020) 101593.
[27] Yasin Amani, Sylvain Dancette, Pauline Delroisse, Aude Simar, Eric Maire, Compression behavior of lattice structures produced by selective laser melting: X-ray tomography based experimental and finite element approaches, Acta Mater. 159 (2018) 395–407.
[28] Jamshid Parvizian, Alexander Düster, Ernst Rank, Finite cell method, Comput. Mech. 41 (1) (2007) 121–133.
[29] Alexander Düster, Ernst Rank, Barna Szabó, The p -version of the finite element and finite cell methods, in: Erwin Stein, René de Borst, Thomas J.R. Hughes (Eds.), Encyclopedia of Computational Mechanics, second edition, John Wiley & Sons, Ltd, 2017, pp. 1–35.
[30] Jean Lemaitre, A continuous damage mechanics model for ductile fracture, J. Eng. Mater. Technol. 107 (1) (1985) 83–89.
[31] Biao Zhang, Yanping Lian, Ming-Jian Li, Chunpeng Wang, Ruxin Gao, Mechanical characterisation of lattice structures fabricated by selective laser melting via an image-based finite cell method with a damage model, Mater. Des. (2024) 113168.
[32] M. Benedetti, V. Fontanari, M. Bandini, F. Zanini, S. Carmignato, Low- and high-cycle fatigue resistance of ti-6al-4v eli additively manufactured via selective laser melting: mean stress and defect sensitivity, Int. J. Fatigue 107 (2018) 96–109.
[33] Erica Liverani, Filippo Zanini, Lavinia Tonelli, Simone Carmignato, Alessandro Fortunato, The influence of geometric defects and microstructure in the simulation of the mechanical behaviour of laser powder-bed fusion components: application to endoprosthesis, J. Manuf. Process. 71 (2021) 541–549.
[34] Filippo Zanini, Marco Sorgato, Enrico Savio, Simone Carmignato, Dimensional verification of metal additively manufactured lattice structures by x-ray computed tomography: use of a newly developed calibrated artefact to achieve metrological traceability, Addit. Manuf. 47 (2021) 102229.
[35] Anton du Plessis, Igor Yadroitsev, Ina Yadroitsava, Stephan G. Le Roux, X-ray microcomputed tomography in additive manufacturing: a review of the current technology and applications, 3D Print. Addit. Manuf. 5 (2018) 227–247.
[36] Herminso Villarraga-Gómez, Ericka L. Herazo, Stuart T. Smith, X-ray computed tomography: from medical imaging to dimensional metrology, Precis. Eng. 60 (2019) 544–569.
[37] J.H. Keyak, J.M. Meagher, H.B. Skinner, C.D. Mote, Automated three-dimensional finite element modelling of bone: a new method, J. Biomed. Eng. 12 (5) (1990) 389–397.
[38] Alexander Düster, Ernst Rank, Barna Aladar Szabó, The p-version of the finite element method and finite cell methods, in: E. Stein, R. Borst, T.J.R. Hughes (Eds.), Encyclopedia of Computational Mechanics, vol. 2, John Wiley & Sons, 2017, pp. 1–35.
[39] Zhengxiong Yang, Martin Ruess, Stefan Kollmannsberger, Alexander Düster, Ernst Rank, An efficient integration technique for the voxel-based finite cell method, Int. J. Numer. Methods Eng. 91 (5) (2012) 457–471.
[40] P. Lazzarin, R. Zambardi, A finite-volume-energy based approach to predict the static and fatigue behavior of components with sharp V-shaped notches, Int. J. Fract. 112 (2001) 275–298.
[41] P. Livieri, P. Lazzarin, Fatigue strength of steel and aluminium welded joints based on generalised stress intensity factors and local strain energy values, Int. J. Fract. 133 (2005) 247–276.
[42] Simone Murchio, Anton Du Plessis, Valerio Luchin, Devid Maniglio, Matteo Benedetti, Influence of mean stress and building orientation on the fatigue properties of sub-unital thin-strut miniaturized ti6al4v specimens additively manufactured via laser-powder bed fusion, Int. J. Fatigue 180 (2024) 108102.
[43] Christopher Derrick, Ali Fatemi, Correlations of fatigue strength of additively manufactured metals with hardness and defect size, Int. J. Fatigue 162 (2022).
[44] S. Romano, A. Brandão, J. Gumpinger, M. Gschweitl, S. Beretta, Qualification of am parts: extreme value statistics applied to tomographic measurements, Mater. Des. 131 (2017) 32–48.
[45] J. Jomo, O. Oztoprak, F. de Prenter, N. Zander, S. Kollmannsberger, E. Rank, Hierarchical multigrid approaches for the finite cell method on uniform and multi-level hp-refined grids, Comput. Methods Appl. Mech. Eng. (2021) 27.
[46] M. Pedranz, V. Fontanari, C. Santus, D. Lusuardi, F. Berto, M. Benedetti, A strain energy density design approach for large cast iron components: from microstructural analysis to multiaxial fatigue response, Int. J. Fatigue 175 (2023).
[47] Alexis Burr, Théo Persenot, Pierre-Thomas Doutre, Jean-Yves Buffiere, Pierre Lhuissier, Guilhem Martin, Rémy Dendievel, A numerical framework to predict the fatigue life of lattice structures built by additive manufacturing, Int. J. Fatigue 139 (2020) 105769.
[48] Raffaele De Biasi, Oguz Oztoprak, Filippo Zanini, Simone Carmignato, Stefan Kollmannsberger, Matteo Benedetti, Fatigue Life Prediction of Am Lattices Based on Image-Based Fcm and Average Strain Energy Density Dataset, 2024.